MATERIALS SCIENCE

3D jet writing of mechanically actuated tandem scaffolds

Seongjun Moon[1,2,3], Michael S. Jones[4], Eunbyeol Seo[1], Jaeyu Lee[1], Lucas Lahann[5], Jacob H. Jordahl[2,6], Kyung Jin Lee[1,2]*, Joerg Lahann[2,4,6,7]*

The need for high-precision microprinting processes that are controllable, scalable, and compatible with different materials persists throughout a range of biomedical fields. Electrospinning techniques offer scalability and compatibility with a wide arsenal of polymers, but typically lack precise three-dimensional (3D) control. We found that charge reversal during 3D jet writing can enable the high-throughput production of precisely engineered 3D structures. The trajectory of the jet is governed by a balance of destabilizing charge-charge repulsion and restorative viscoelastic forces. The reversal of the voltage polarity lowers the net surface potential carried by the jet and thus dampens the occurrence of bending instabilities typically observed during conventional electrospinning. In the absence of bending instabilities, precise deposition of polymer fibers becomes attainable. The same principles can be applied to 3D jet writing using an array of needles resulting in complex composite materials that undergo reversible shape transitions due to their unprecedented structural control.

INTRODUCTION

Three-dimensional (3D) microprinting has attracted scientific and technological interest for decades, and recent technological innovation related to the development of 3D micromanufacturing techniques has established intriguing pathways for producing controlled 3D scaffolds composed of diverse material combinations (*1*–*3*). These materials—including metals, ceramics, polymers, and even concrete—have been adopted for a wide array of 3D printing applications. In particular, 3D printing of microscopically controlled scaffold architectures from polymer materials has been demonstrated using a range of different techniques, including melt-spinning (*4*), dot-printing (*5*, *6*), stereolithography (*7*–*9*), or selective laser sintering (*10*, *11*). Tailored, preprogrammed 3D architectures can be fabricated by optimizing the rheology of polymer solutions (or melt), such as the balance of their respective discharge and coagulation rates (*12*). However, there are inherent limitations, such as nozzle-out swelling or mismatched surface tensions, that prevent further reduction of the dimensions of polymer threads below 50 μm by simply adjusting a solution's rheological properties alone (*13*).

Electrospinning presents an excellent approach for reducing the diameter of the polymer thread to micrometer and even nanometer dimensions. However, in general, electrospinning produces 2D, randomly oriented nonwoven fiber mats, and the resulting structures generally lack organization and widespread adoption of electrospinning as a 3D microprinting technology has been challenging because of the inherently complex electrohydrodynamic effects that prevent precise control of the depositing jet (*14*, *15*). In recent years, examples have emerged, such as melt electrowriting (*16*–*19*), solution jet writing (*20*), and near-field electrospinning (*21*), where spatial 3D definition has been achieved, and some of these methods—typically optimized for a specific polymer—have already found broader applications.

In conventional electrojetting, the counter electrode is grounded and the needle carries a positive surface potential. This configuration results in a radial electric field that is formed within the needle and acts upon charge carriers present in the jetting solution. Electrons and cations, the main types of charger carriers of the jetting solution, are accelerated differently in the radial electrical field, simply because their masses differ by several orders of magnitude. In the regular jetting setup, the electrons are accelerated from the bulk solution toward the interface. Smaller charge carriers are moving faster than cations with a larger mass to reach the needle interface during the extremely short time scales of electrospinning, ultimately giving rise to a higher net surface potential of the ejected electrified jet (*22*).

Herein, we report a process for microprinting of 3D microarchitectures using a modified electrospinning approach, i.e., 3D jet writing that takes advantage of the concept of charge reversal (*22*–*25*). Compared to conventional electrospinning, our system effectively suppresses whipping instabilities of polymeric jet by reducing the net surface charge of the electrohydrodynamic jet. Our work further demonstrates that parallelized processing of precisely matched combinations of polymer solutions can result in complex, shape-shifting tandem scaffolds.

RESULTS

Charge-reversed electro-jet writing system to build 3D micro-structure

Figure 1 shows a diagram of the charge-reversed electro-jet writing (CREW) process. Polymer solutions are prepared with concentration ranging from 10 to 70 w/v % with diverse solvent compositions. The factors governing the choice of appropriate solvent combinations include the following: (i) the solvent should be able to dissolve polymers with reasonable viscosity [1000 to 1200 centipoise (cps)] in this setup,

[1]Department of Chemical Engineering and Applied Chemistry, College of Engineering, Chungnam National University, 99 Daehak-ro (st), Yuseong-gu, Daejeon 305-764, Republic of Korea. [2]Department of Chemical Engineering, University of Michigan, Ann Arbor, MI 48109, USA. [3]Information and Electronics Research Institute, Korea Advanced Institute of Science and Technology (KAIST), 291 Daehak-ro, Yuseong-gu, Daejeon 34141, Republic of Korea. [4]Macromolecular Science and Engineering, University of Michigan, Ann Arbor, MI 48109, USA. [5]Department of Electrical Engineering, University of Michigan, Ann Arbor, MI 48109, USA. [6]Biointerfaces Institute, University of Michigan, Ann Arbor, MI 48109, USA. [7]Institute of Functional Interfaces, Karlsruhe Institute of Technology, 76344 Eggenstein-Leopoldshafen, Germany.
*Corresponding author. Email: kjlee@cnu.ac.kr (K.J.L.); lahann@umich.edu (J.L.)

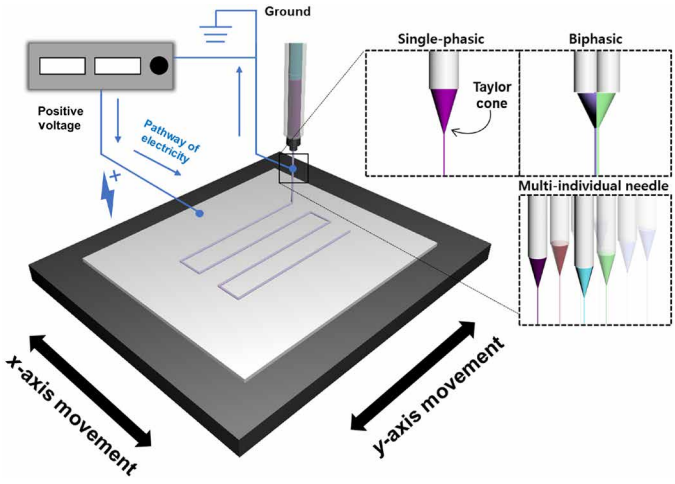

Fig. 1. Schematic diagram of the CREW system. The CREW system for fabrication of a fiber-based scaffold using the moving stage. The positive voltages are applied to the conductive collector. The blue lines represent pathway of electricity.

and (ii) the evaporation rate is not too fast or slow, so that the solidification is possible or the needle is not clogged during the writing. A positive voltage around 2 to 5 kV is applied to the collector (*20*, *26*–*29*). Once the jet-launching is stabilized, one can obtain a 3D microarchitecture drawn with an approximately 10-μm level of polymer fiber threads using the moving stage. Experimentally, this approach differs from more conventional configurations (*20*, *30*–*32*) in that the positive charge is applied onto a movable substrate.

By reducing the net electrical potential of the ejected jet, we effectively favor the dampening viscoelastic forces over repulsive coulomb forces, suppress the onset of bending instabilities, and enable the preparation of precisely defined 3D fiber structures. Figure 2A shows a photograph of the Taylor cone formed during jetting of a poly(lactic-co-glycolic acid) (PLGA) solution at only 3 kV. The electrified jet ejected from the tip of the needle is stable, devoid of any discernable signs of bending instabilities.

Compared to conventional electrospinning, bending instabilities of the electrified jet can be notably reduced during the CREW process. On the basis of the charge reversal, the needle will carry an induced negative polarity, resulting in the acceleration of cations, rather than electrons toward the needle wall. The lower transport velocity of larger cations and low density of the induced negative charge will result in a lower net interfacial charge of the jetting solution (see figs. S1 and S2) (*22*). Once the electrified jet is ejected from the Taylor cone, the trajectory of the jet is affected by the balance of charge-charge repulsion and viscoelastic forces. Bending instabilities initially originate from small perturbations of the jet resulting in the loss of axial symmetry. The extent of the outward trajectory is enhanced by coulomb repulsion but compensated by viscoelastic forces inherent to the jetting solution. Thus, the magnitude of the net surface charge of the electrified jet is critical, as it determines the formation and growth factor of the bending instabilities. Brenner and colleagues have rigorously established existence criteria for the formation of bending instabilities (*33*–*37*). According to Yarin *et al.*, the force in the axial direction on a certain element of the jet with length 2*L* can be described by the following equation

$$\boldsymbol{F}_{\mathrm{ax}} = -\sigma^2 \ln\left(\frac{L}{a}\right)|k|\,\boldsymbol{n}\mathrm{d}\zeta \quad (1)$$

where σ represents the charge per unit length of the jet, the cross-sectional radius of the jet is denoted as *a*, the curvature of the element is denoted by *k*, ***n*** is a unit vector perpendicular to the unperturbed centerline of the jet, and ζ is an arc length of jet (*38*). Qualitatively, the reduction in net charge of the electrified jet during reverse electrospinning will reduce the coulomb repulsion forces (figs. S1 and S2) and dampens or even completely eliminates the onset of bending instabilities. In our work, we found that a reversed applied voltage as low as 3 kV (1-cm gap, Fig. 2) resulted in a straight jet trajectory devoid of any apparent whipping instabilities. Because the onset of instabilities is suppressed under these conditions, multiplexed needle configurations can be implemented that lead to both complex, compartmentalized architectures and higher-throughput production.

Figure 2B presents an example of electrohydrodynamic cojetting with two different polymer solutions—thermoplastic polyurethane (TPU) and PLGA. Although these two polymers have quite different molecular structures and thus distinct chemical, physical, and electrohydrodynamic properties, a stable singular Taylor cone was obtained. The jet's whipping motion was suppressed as it is launched from the Taylor cone. The driving force for whipping motions is built up of extra interfacial charges in the traveling polymer jet (*39*). In conventional electrojetting, electrons are quickly removed from the jetting solution under the strong radial electric field induced upon application of the voltage. As evidenced by Eq. 1, the jetted solution thus carries a positive charge, resulting in strong coulomb repulsion (Fig. 2C). Because of the higher surface potential, the repulsive forces overcome the dampening viscoelastic forces and cause chaotic whipping of the jet (Fig. 2D and fig. S3A). On the other hand, in the charge reversed electrojetting system, heavier cations, rather than electrons, move toward the negatively polarized wall, resulting in a lower net potential of the electrified jet (Fig. 2E). This charge density becomes low enough that the dampening forces can dominate the axially directed, repulsive coulomb forces. Consequently, the onset of bending instabilities is effectively suppressed, giving rise to well-ordered 3D structures that are prepared under otherwise identical conditions (Fig. 2F and fig. S3B).

3D jet writing

The CREW system—stabilized by reduced whipping motion and electrical convergence—makes it possible to draw precise 3D architectures with a polymer thread, as represented in several precedent works (*6*, *20*, *40*). Figure 3 shows a 3D-written triangular structure and a honeycomb structure (sketches for the movement of the stage are provided in fig. S4) using a PLGA jetting solution. During the fiber stacking (here, a stack of 10 microfibers), individual fibers appear to be close-to-perfectly aligned. The diameter of single fibers is in the range of 10 μm, which is similar to that of our previous work (*20*). The diameter of a single fiber can be controlled by adjusting the applied voltage, the feed rate of the polymer solution(s), the concentration of polymer solution(s), and the moving speed of the counter electrode. Complex grid structures are successfully generated as shown in Fig. 3 (B and D) by 3D stacking of the polymer fiber jet. 3D stacking of polymer fibers into curved structures is also possible because of the stable, nonwhipping jet created with CREW. Printing the entire structures required more than 30 min, during which the fiber quality remained consistent, implying that

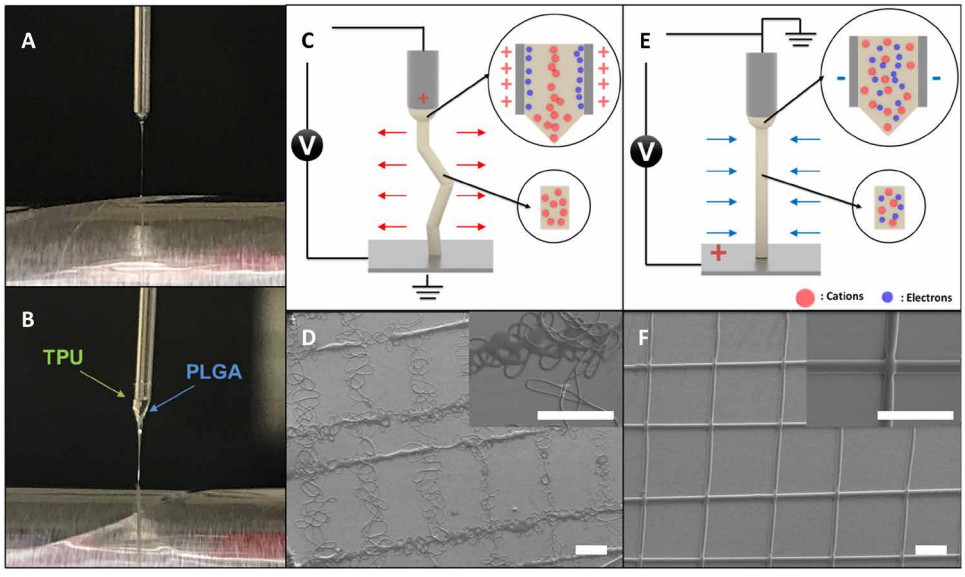

Fig. 2. Mechanism of a straight jet. Digital images of Taylor cones for (**A**) a single-phasic microfiber and (**B**) a biphasic microfiber. PLGA was used for the single-phasic microfiber; PLGA and TPU were used for the biphasic microfiber. Schematic diagrams of the forces applied to the polymeric jet for (**C**) the conventional jetting system and (**E**) the CREW system. SEM images of grid patterns that are produced by (**D**) the conventional jetting system and (**F**) the CREW system. Scale bars, 300 μm. (Photo credit: Seongjun Moon, Chungnam National University.)

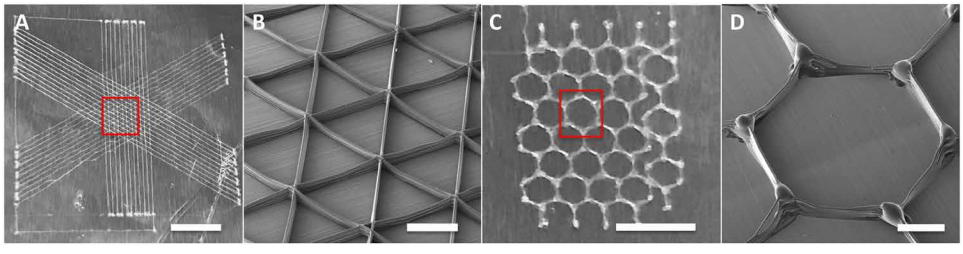

Fig. 3. 3D printed patterns. Digital images of 3D printed structures prepared by the CREW system representing (**A**) a triangular structure and (**C**) honeycomb. (**B** and **D**) SEM of selected parts of these 3D printed structures. Scale bars, 500 μm.

there is little deterioration of the jetting process over time. Not only is 3D jet writing with the CREW system versatile in terms of shape and geometry of target architecture, but the dimensions of single fiber are smaller than that of commercially available 3D printing systems that have adopted polymer thread as a basic component.

Material diversity and 3D construction of heterogeneous polymer scaffolds

Production of 3D printed objects with different types of materials is of broad interest; however, it is typically difficult as it requires tedious optimization (*41*). In the case of electrical field–assisted 3D writing, many experimental parameters have a strong influence on jetting behavior (*42*, *43*). Typically, most of these parameters are classified into two types (*39*, *44*): (i) internal parameters (mainly properties of the polymer solution), such as viscosity, solvent properties, molecular weight of polymer, conductivity, and surface tension, and (ii) external parameters (mainly operating parameters) including applied voltage, gap distance, flow rate, and collecting speed. Furthermore, it has been shown that changing internal parameters affects external parameters, and thus, tedious reoptimization is required to adapt a system to these changes (*39*). However, when the type of polymer is varied, a number of internal parameters can change to the point where it becomes impossible to replicate the same jetting conditions by manipulating the external conditions alone. In addition, accumulated charges in the polymer solution can maximize the complexity of adjusting these parameters. As previously mentioned, however, because positive charges are applied onto the collector, the electrohydrodynamic effect on the solution will be minimized as long as the pulling interaction is maintained. Therefore, diverse types of polymer solutions can be readily adopted without the need for tedious optimization. Figure 4 shows scanning electron microscopy (SEM) images of 3D printed scaffolds made of different polymers: TPU, azide TPU, PLGA, polycaprolactone (PCL), poly(methyl methacrylate) (PMMA), poly(vinyl cinnamate) (PVCi), and poly(hydroxyl butylate) (PHB). Several of the internal and external parameters are summarized in Table 1. Although each polymer jetting solution—in terms of both the polymer type and the composition of its corresponding solvent system—is compositionally distinct, similar jet behavior was observed, allowing us to use nearly identical experimental parameters. The 3D shape and thickness of single polymer threads are also very similar (the average fiber diameters can be adjusted to 10 μm by

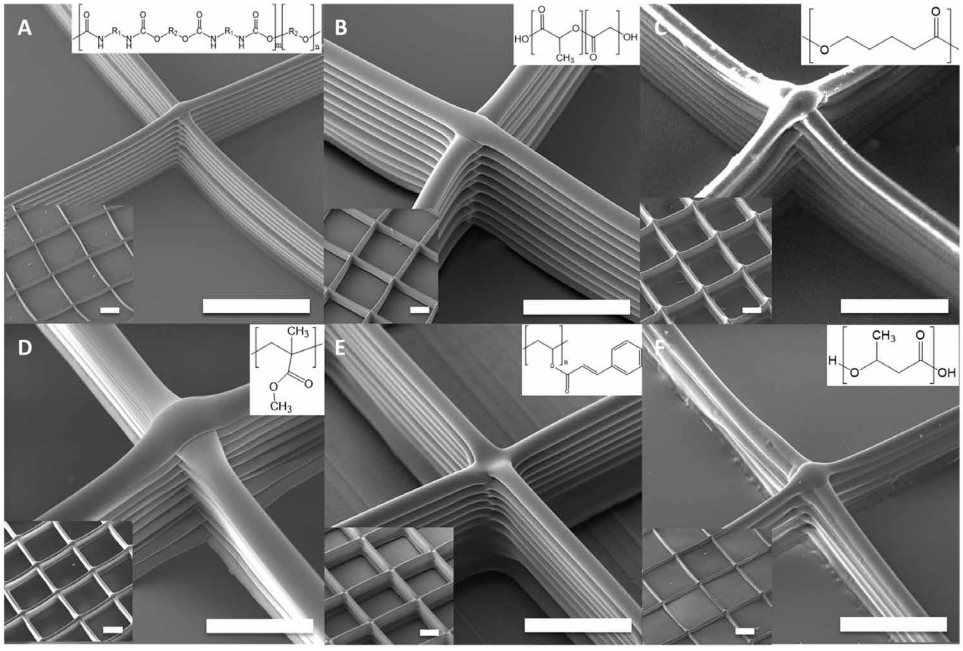

Fig. 4. Material diversity. SEM images of scaffolds prepared using various polymer materials by the CREW system. (**A**) TPU, (**B**) PLGA, (**C**) PCL, (**D**) PMMA, (**E**) PVCi, and (**F**) PHB were used as polymer materials, and the THF/DMF pair was used for (A) to (E) as solvent to prepare the polymer solutions, and the TFE/chloroform pair was used for (F). Scale bars, 200 μm.

Table 1. Internal and external parameters for the CREW system.

Materials	Solvents (%)	Concentration (w/v %)	Applied voltage (kV)	Feed rate (μl/h)	Stage moving rate (μm/s)
TPU	60:40 THF/DMF	20	2.5	70	48
PLGA	70:30 THF/DMF	70	3.0	70	50
PCL	60:40 THF/DMF	50	3.0	100	50
PMMA	50:50 THF/DMF	40	3.0	70	50
PVCi	60:40 THF/DMF	70	3.0	110	50
PHB	70:30 TFE/chloroform	10	2.7	90	50

precisely controlling the jetting parameters), implying a significant degree of versatility. The need to optimize external parameters is thus minimized in this system, and almost identical microarchitectures and even more complex structures can be fabricated when the viscosity of polymer solution is within a defined range (1000 to 1200 cps). This study successfully establishes the preparation of 3D scaffolds composed of different types of polymers.

The CREW process has the potential to greatly extend the possible application fields of polymer 3D architecture, even using several polymers provided here as representative examples—PLGA and PCL for biodegradable 3D scaffold, TPU for flexible 3D architecture, and PVCi for cross-linkable polymer (*45*). In particular, the bio-derived polymer PHB provides fascinating application fields through selective binding of proteins or enzyme for smart scaffolds and microsupporters (*46*, *47*). As an example, the "M" pattern and the star structure were printed as shown in fig. S5 (A and B) from PMMA, which is an example of a stiff polymer, and TPU, being a more flexible polymer (70 stacks each). Although the properties of these polymers are different, the CREW process yielded macroscopic architectures that matched the intended design. In addition, our system could not only provide 3D architecture using single polymer thread (ca. 10 to 20 μm; it can be varied by controlling either concentration or several experimental parameters) but also allow for stacking of different types of polymers on a predefined location (fig. S5, C and D). The tandem structure was formed by a first layer of TPU with 60 stacks (fig. S5C) followed by a second layer of PMMA writing with 30 stacks on top of it to fill the structures (fig. S5D). The printing accuracy characteristically depends on the distance from the substrate and can be controlled by adjusting the voltage applied to the substrate (*48*). These 3D structures printed with multicomponents can provide versatility in designing 3D printed objects. The high resolution and material diversity of the CREW system make it possible to prepare preprogrammed thermo-driven origami architectures with macroscopic resolution. Here, to mimic the flower motion, a bilayer flower pattern was prepared using a PLGA jet printed onto a PMMA flower pattern

(Fig. 5A). The different thermal expansion of the PLGA and PMMA microfibers at 80°C causes a directed bending motion, leading to controlled actuation of the entire structure in a highly controllable manner (Fig. 5B). As demonstrated in Fig. 5 (C to F), the bending behavior can be precisely adjusted by applying different patterns (see fig. S6 for pattern) created by printing a second layer (PLGA).

Compared to general jetting systems such as near-field electrospinning, melt-electrospinning, and electrohydrodynamic (EHD) jetting, the CREW process can be easily combined with conventional 3D printing technology (fig. S7 and table S1) (*20*, *30*–*32*, *49*). The integration of the CREW system into a conventional 3D printer can decrease the feature size by more than 10 times. Figure S8 (A and B) shows the SEM image of 3D structures prepared by the 3D printer itself and the CREW system mounted on a conventional 3D printer. The structures printed by the CREW system shows much smaller diameters than those made by conventional 3D printing, while the exact same shapes of the 3D printed structure can be obtained (fig. S8, C and D). Future work will aim at expanding the CREW system to a broader range of biomedical or soft electronics applications (*50*, *51*).

Configuration of microstructure

The CREW process tends to minimize competing electrohydrodynamic effects that stem from a mismatch among different polymer solutions as described in Fig. 2B. Therefore, the composition of the polymer thread, which constitutes the basic component of 3D architecture, is not constrained to one single material, but rather can be extended to biphasic threads and may even allow for accessing higher-order permutations of materials within a single fiber thread (*52*). Previously, we have adopted a dual core-shell system followed by shell removal to obtain Janus microfibers or cylinders composed of a mixture of totally different polymers (*28*, *29*, *52*). The sacrificial shell had been crucial in reducing the electrohydrodynamic effect from each polymer solution. However, biphasic jetting is possible without using the shell system by instead using the CREW approach. 3D writing of biphasic jetting has been successfully carried out. Figure 6 shows several confocal laser scanning microscope (CLSM) images of biphasic fiber stacking. Fiber pairs of PLGA/TPU, PMMA/TPU, PMMA/PLGA, PLGA/PVCi, and TPU/ATPU (see fig. S9 in detail) (*53*) are displayed as representative examples. Note that this method can be extended to different types of polymer beyond the examples provided in Fig. 6. The 3D printed object can not only have multiple compartments composed of different polymers but also contain specific micrometer-scale geometries such as triphasic architectures (*54*–*57*). Therefore, 3D microstructures can be endowed with diverse and desired physical and chemical properties. For instance, additional functionalities can be easily introduced via surface treatment. Surface treatment of azido groups can be spatioselectively carried out using a click reaction onto Janus 3D microarchitectures. Figure 6E shows a CLSM image of biphasic microfibers in which one side is composed of TPU and the other is composed of ATPU. The half-filled green color comes from the green fluorescent dye introduced into the TPU solution. The azido groups on one compartment (ATPU) can be used for the surface reaction; here,

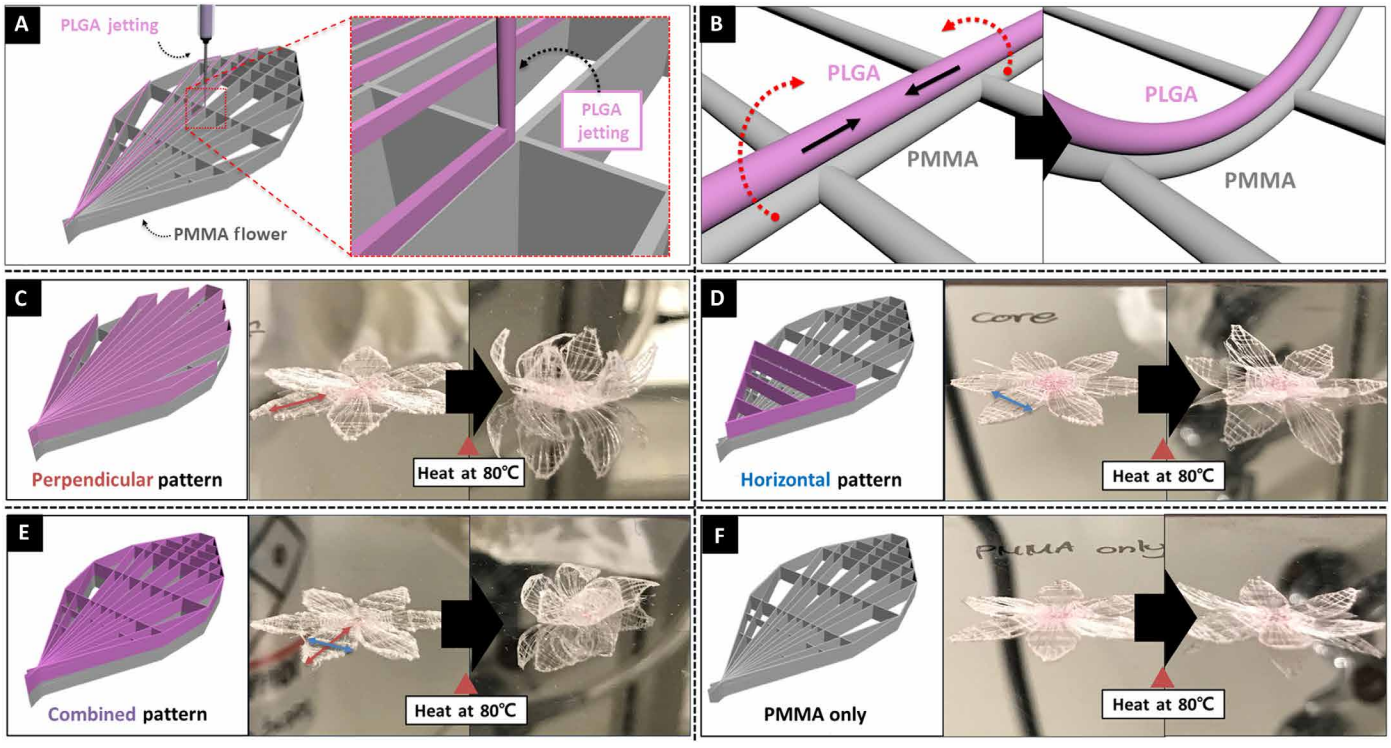

Fig. 5. Tandem scaffold. (**A**) Schematic diagram of the design of tandem scaffolds using PMMA and PLGA, where the PLGA was precisely positioned onto a PMMA pattern; (**B**) schematic diagram of the mechanism of bending motion of a PLGA/PMMA bilayered pattern at elevated temperature (here, 80°C); schematic diagram and digital photo of before and after heat treatment depending on its PLGA pattern, (**C**) perpendicular pattern, (**D**) horizontal pattern, (**E**) combined pattern, and (**F**) PMMA only. (Photo credit: Seongjun Moon, Chungnam National University.)

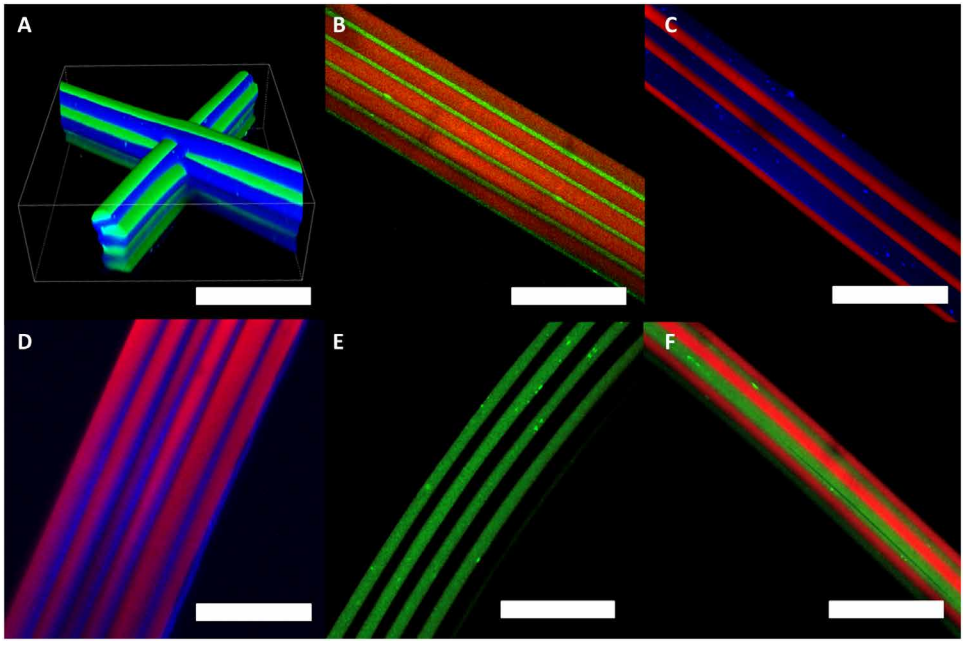

Fig. 6. Configuration of microstructure. (**A**) 3D confocal laser scanning microscope image of a PLGA/TPU biphasic scaffold. The blue dye and the green dye represent PLGA and TPU, respectively. (**B** to **E**) Confocal microscope images of biphasic microfibers using various polymer pairs. (B) PMMA/TPU (red/green), (C) PMMA/PLGA (red/blue), and (D) PLGA/PVCi (blue/red). All colors represent organic dyes used to label the respective polymer solutions. (E) Confocal microscope image of TPU (green dye)/ATPU, which has azide groups in its chemical structure. (**F**) Confocal microscope image of TPU/ATPU biphasic microfiber after azide-alkyne click reaction with alkyne-spiropyran. The green dye represents the TPU and the red dye represents the conjugated spiropyran. Scale bars, 100 μm.

spiropyran, which contains reactive triple bonds (fig. S9), is selectively anchored on one side of the scaffold (fig. S10 and Fig. 5F). In this configuration, a reversible photochromic response can be observed, implying successful and easy anchoring of an external chemical onto the scaffold (fig. S11).

Parallelized production

Last, the CREW process provides benefits in terms of high-throughput production compared to the previous system. It is generally difficult to expand electrospinning methods into multinozzle systems because increasing the number of needles will induce electrical interference between individual nozzles (*15*, *58*–*60*). However, here, because the voltage is applied to the collector, it is possible to increase the number of needles, while avoiding substantial interferences between the parallel polymer jets. As described in Fig. 7A, each needle maintains a stable jet required for 3D jet writing despite being in proximity (as low as 5 mm) to other needles. In addition, various polymer solutions can be simultaneously adopted in each needle during jet writing as shown in Fig. 7B. The polymer threads from each needle had close-to-identical shapes in terms of thickness and 3D stacking, judging from each SEM image. In addition, simultaneous jets can be extended to establish a parallel 3D jet writing configuration, resulting in higher-throughput production (fig. S12 and video S1). PMMA, TPU, and PLGA were introduced into separate needles as shown in fig. S12. In this configuration, multiple scaffolds were successively prepared without any deterioration on the process or product.

DISCUSSION

Here, we introduce the CREW method as a step toward a more universal 3D microprinting technology that establishes a major departure from electrospinning. This approach allows for writing of polymer microfibers into precisely controlled architectures, mostly due to the effective suppression of the electrohydrodynamic effect and minimization of whipping motion during electrohydrodynamic jetting. Without substantial changes to the CREW process, 3D printed polymer architectures from various polymer materials and combination were obtained. Furthermore, high-throughput production of polymer microfibers is possible, because the reduced voltage applied to the jetting solution minimizes the electrical interference between parallel nozzles and thus lends itself to printing with arrays of nozzles. Although the current process is carried out in a laboratory-scale apparatus, the CREW process may benefit from the inclusion of a temperature control, microfluidic nozzle design, and integration with established printer technology, which should further improve the precision and versatility of the process. With further work, the CREW process should establish a major scientific and technological breakthrough toward a deployable, robust, and scalable 3D printing technique based on electrohydrodynamic jetting. We envision this methodology to be adopted in the production of various 3D architectures that may be composed of multiple polymers, or be anisotropically configured into Janus-type, coaxial, or tricompartmental polymer threads.

MATERIALS AND METHODS

Reagent and materials

PLGA (ester-terminated, M_w 50,000 to 75,000 g mol^{-1}), PCL (average M_w ~65,000, average M_n ~42,500, pellets), PMMA [average M_w ~120,000 by gel permeation chromatography (GPC)], poly[(*R*)-3-hydroxybutyric acid] (natural origin) (PHB), PVCi (average M_w ~200,000 by GPC, powder), tetrahydrofuran (THF) [anhydrous,

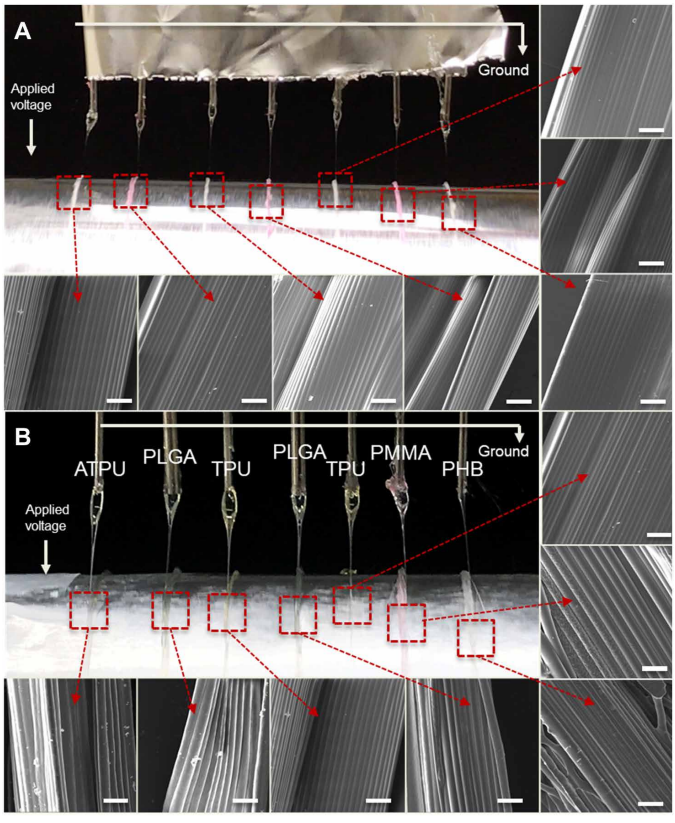

Fig. 7. Parallelized production. Digital images of the Taylor cones of seven polymer jets and SEM images of obtained microfiber bundles using seven needles in parallel (**A**) with TPU in the THF/DMF mixture with red and green dyes and (**B**) with various polymer materials such as the ATPU, PLGA, TPU, and PMMA in the THF/DMF mixture, and PHB in the chloroform/DMF mixture. Scale bars, 100 μm. (Photo credit: Seongjun Moon, Chungnam National University.)

contains 250 parts per million (ppm) butylated hydroxytoluene (BHT) as inhibitor, ≥99.9%], *N*,*N*′-dimethylformamide (DMF) (ReagentPlus, ≥99%), chloroform (contains 100 to 200 ppm amylenes as stabilizer, ≥99.5%), Rhodamine B isothiocyanate (mixed isomers) (red dye), poly[(m-phenylenevinylene)-alt-(2,5-dihexyloxy-*p*-phenylenevinylene)] (MEHPV), poly[tris(2,5-bis(hexyloxy)-1,4-phenylenevinylene)-alt-(1,3-phenylenevinylene)] (PTDPV), and (+)-sodium L-ascorbate (powder, Bioreagent, suitable for cell culture) (NaAs) were purchased from Sigma-Aldrich, USA. Copper (II) sulfate pentahydrate (98+%, ACS reagent) was purchased from Acros Organics, USA. TPU (Neothane) was purchased from DongSung Corp., Republic of Korea. In addition, ATPU and ultraviolet-detectable chromic dye were prepared; refer to our previous report (*53*).

Preparation of microfiber

The CREW system was conducted with a high DC voltage applier (Gamma High Voltage Research, ES30P-20W), a polymer solution, a syringe, a syringe pump (Thermo Fisher Scientific), a precise needle (23 G or 21 G), and a conductive collector. The syringe pump, with the syringe and the precise needle, was located above a conductive collector, which consists of a stainless steel plate or aluminum foil. The high DC voltage was applied onto the conductive collector. The polymer solutions were continuously injected by the syringe pump, and then the polymer jet was launched onto the conductive collector by the applied high voltage. To stabilize environmental condition and minimize the skin formation on jet, the entire process was carried out in a humidity-controlled room with 35% relative humidity and a temperature of 24°C. Two linear motion stages were implemented to make the scaffold, one stage for x and y motion, respectively (ILS-300LM, Newport Corporation). A four-axis universal controller (XPS-Q4, Newport Corporation) coupled with LabView software synchronized the stage movements.

Preparation of biphasic microfiber

The specific compositions of the jetting solutions are shown in Table 1. Each compartment contained a different fluorescent dye (red dye, MEHPV, and PTDPV) at a concentration <0.01 w/v %. Jetting solutions were loaded into syringe and pumped through a side-by-side needle via a syringe pump. The needle was placed 0.5 to 1 cm above the collector. Normally, 2.5 to 3 kV of voltage was applied to the conductive collector. Fibers were jetted onto a conductive collector.

Characterization

The morphology of the microfibers and the scaffold was confirmed using TESCAN MIRA3 FEG (field emission gun)–SEM from TESCAN. In the case of CLSM, the images were obtained using an A1R HD instrument from Nikon. The separated colors were collected using the MEHPV, the PTDPV, and the red dye representing blue color, green color, and red color, respectively. In addition, the NIS-Elements viewer from Nikon was used to visualize the 3D confocal image.

SUPPLEMENTARY MATERIALS

Supplementary material for this article is available at http://advances.sciencemag.org/cgi/content/full/7/16/eabf5289/DC1

REFERENCES AND NOTES

1. E. Y. Heo, N. R. Ko, M. S. Bae, S. J. Lee, B.-J. Choi, J. H. Kim, H. K. Kim, S. A. Park, I. K. Kwon, Novel 3D printed alginate–BFP1 hybrid scaffolds for enhanced bone regeneration. *J. Ind. Eng. Chem.* **45**, 61–67 (2017).
2. J. Wang, T. Lu, M. Yang, D. Sun, Y. Xia, T. Wang, Hydrogel 3D printing with the capacitor edge effect. *Sci. Adv.* **5**, eaau8769 (2019).
3. Y.-G. Park, H. S. An, J.-Y. Kim, J.-U. Park, High-resolution, reconfigurable printing of liquid metals with three-dimensional structures. *Sci. Adv.* **5**, eaaw2844 (2019).
4. L. Cui, N. Zhang, W. Cui, P. Zhang, X. Chen, A novel nano/micro-fibrous scaffold by melt-spinning method for bone tissue engineering. *J. Bionic Eng.* **12**, 117–128 (2015).
5. Y. H. Yun, J. D. Kim, B. K. Lee, Y. W. Cho, H. Y. Lee, Polymer inkjet printing: Construction of three-dimensional structures at micro-scale by repeated lamination. *Macromol. Res.* **17**, 197–202 (2009).
6. J.-U. Park, M. Hardy, S. J. Kang, K. Barton, K. Adair, D. k. Mukhopadhyay, C. Y. Lee, M. S. Strano, A. G. Alleyne, J. G. Georgiadis, P. M. Ferreira, J. A. Rogers, High-resolution electrohydrodynamic jet printing. *Nat. Mater.* **6**, 782–789 (2007).
7. J. Z. Manapat, Q. Chen, P. Ye, R. C. Advincula, 3D printing of polymer nanocomposites via stereolithography. *Macromol. Mater. Eng.* **302**, 1600553 (2017).
8. H. Kwak, S. Shin, H. Lee, J. Hyun, Formation of a keratin layer with silk fibroin-polyethylene glycol composite hydrogel fabricated by digital light processing 3D printing. *J. Ind. Eng. Chem.* **72**, 232–240 (2019).
9. Y. Yang, X. Li, M. Chu, H. Sun, J. Jin, K. Yu, Q. Wang, Q. Zhou, Y. Chen, Electrically assisted 3D printing of nacre-inspired structures with self-sensing capability. *Sci. Adv.* **5**, eaau9490 (2019).
10. S. F. S. Shirazi, S. Gharehkhani, M. Mehrali, H. Yarmand, H. S. C. Metselaar, N. Adib Kadri, N. A. A. Osman, A review on powder-based additive manufacturing for tissue engineering: Selective laser sintering and inkjet 3D printing. *Sci. Technol. Adv. Mater.* **16**, 033502 (2016).
11. F. Fina, A. Goyanes, S. Gaisford, A. W. Basit, Selective laser sintering (SLS) 3D printing of medicines. *Int. J. Pharm.* **529**, 285–293 (2017).
12. S. C. Ligon, R. Liska, J. Stampfl, M. Gurr, R. Mülhaupt, Polymers for 3D printing and customized additive manufacturing. *Chem. Rev.* **117**, 10212–10290 (2017).

13. T. D. Ngo, A. Kashani, G. Imbalzano, K. T. Q. Nguyen, D. Hui, Additive manufacturing (3D printing): A review of materials, methods, applications and challenges. *Compos. Part B Eng.* **143**, 172–196 (2018).
14. J. Xue, J. Xie, W. Liu, Y. Xia, Electrospun nanofibers: New concepts, materials, and applications. *Acc. Chem. Res.* **50**, 1976–1987 (2017).
15. J. H. Jordahl, S. Ramcharan, J. V. Gregory, J. Lahann, Needleless electrohydrodynamic cojetting of bicompartmental particles and fibers from an extended fluid interface. *Macromol. Rapid Commun.* **38**, 1600437 (2017).
16. G. Hochleitner, T. Jüngst, T. D. Brown, K. Hahn, C. Moseke, F. Jakob, P. D. Dalton, J. Groll, Additive manufacturing of scaffolds with sub-micron filaments via melt electrospinning writing. *Biofabrication* **7**, 035002 (2015).
17. T. D. Brown, P. D. Dalton, D. W. Hutmacher, Direct writing by way of melt electrospinning. *Adv. Mater.* **23**, 5651–5657 (2011).
18. I. Liashenko, A. Hrynevich, P. D. Dalton, Designing outside the box: Unlocking the geometric freedom of melt electrowriting using microscale layer shifting. *Adv. Mater.* **32**, 2001874 (2020).
19. I. Liashenko, J. Rosell-Llompart, A. Cabot, Ultrafast 3D printing with submicrometer features using electrostatic jet deflection. *Nat. Commun.* **11**, 753 (2020).
20. J. H. Jordahl, L. Solorio, H. Sun, S. Ramcharan, C. B. Teeple, H. R. Haley, K. J. Lee, T. W. Eyster, G. D. Luker, P. H. Krebsbach, J. Lahann, 3D jet writing: Functional microtissues based on tessellated scaffold architectures. *Adv. Mater.* **30**, 1707196 (2018).
21. D. Sun, C. Chang, S. Li, L. Lin, Near-field electrospinning. *Nano Lett.* **6**, 839–842 (2006).
22. Z. Li, R. Liu, Y. Huang, J. Zhou, Effects of reversed arrangement of electrodes on electrospun nanofibers. *J. Appl. Polym. Sci.* **134**, 44687 (2017).
23. U. Ali, X. Wang, T. Lin, Effect of nozzle polarity and connection on electrospinning of polyacrylonitrile nanofibers. *J. Text. Inst.* **103**, 1160–1168 (2012).
24. A. Kilic, F. Oruc, A. Demir, Effects of polarity on electrospinning process. *Text. Res. J.* **78**, 532–539 (2008).
25. Z. Li, H. Kang, N. Che, Z. Liu, P. Li, W. Li, C. Zhang, C. Cao, R. Liu, Y. Huang, Effects of electrode reversal on the distribution of naproxen in the electrospun cellulose acetate nanofibers. *J. Nanomater.* **2014**, 360658 (2014).
26. M. Gil, S. Moon, J. Yoon, S. Rhamani, J.-W. Shin, K. J. Lee, J. Lahann, Compartmentalized microhelices prepared via electrohydrodynamic cojetting. *Adv. Sci.* **5**, 1800024 (2018).
27. J. Lee, T.-H. Park, K. J. Lee, J. Lahann, Snail-like particles from compartmentalized microfibers. *Macromol. Rapid Commun.* **37**, 73–78 (2016).
28. K. J. Lee, T.-H. Park, S. Hwang, J. Yoon, J. Lahann, Janus-core and shell microfibers. *Langmuir* **29**, 6181–6186 (2013).
29. K. J. Lee, J. Yoon, S. Rahmani, S. Hwang, S. Bhaskar, S. Mitragotri, J. Lahann, Spontaneous shape reconfigurations in multicompartmental microcylinders. *Proc. Natl. Acad. Sci.* **109**, 16057–16062 (2012).
30. C. Chang, K. Limkrailassiri, L. Lin, Continuous near-field electrospinning for large area deposition of orderly nanofiber patterns. *Appl. Phys. Lett.* **93**, 123111 (2008).
31. C. Chang, V. H. Tran, J. Wang, Y.-K. Fuh, L. Lin, Direct-write piezoelectric polymeric nanogenerator with high energy conversion efficiency. *Nano Lett.* **10**, 726–731 (2010).
32. T.-S. Kim, Y. Lee, W. Xu, Y. Kim, M. Kim, S.-Y. Min, T. Kim, H. Jang, T. W. Lee, Direct-printed nanoscale metal-oxide-wire electronics. *Nano Energy* **58**, 437–446 (2019).
33. M. M. Hohman, M. Shin, G. Rutledge, M. P. Brenner, Electrospinning and electrically forced jets. I. Stability theory. *Phys. Fluids* **13**, 2201–2220 (2001).
34. H. Yuan, Q. Zhou, Y. Zhang, 6—Improving fiber alignment during electrospinning, in *Electrospun Nanofibers*, M. Afshari, Ed. (Woodhead Publishing, 2017), pp. 125–147.
35. M. Yousefzadeh, 12—Modeling and simulation of the electrospinning process, in *Electrospun Nanofibers*, M. Afshari, Ed. (Woodhead Publishing, 2017), pp. 277–301.
36. Y. M. Shin, M. M. Hohman, M. P. Brenner, G. C. Rutledge, Experimental characterization of electrospinning: The electrically forced jet and instabilities. *Polymer* **42**, 09955–09967 (2001).
37. D. H. Reneker, A. L. Yarin, H. Fong, S. Koombhongse, Bending instability of electrically charged liquid jets of polymer solutions in electrospinning. *J. Appl. Phys.* **87**, 4531–4547 (2000).
38. A. L. Yarin, S. Koombhongse, D. H. Reneker, Bending instability in electrospinning of nanofibers. *J. Appl. Phys.* **89**, 3018–3026 (2001).
39. A. L. Andrady, *Science and Technology of Polymer Nanofibers* (John Wiley & Sons, 2008).
40. P. Fattahi, J. T. Dover, J. L. Brown, 3D near-field electrospinning of biomaterial microfibers with potential for blended microfiber-cell-loaded gel composite structures. *Adv. Healthc. Mater.* **6**, 10.1002/adhm.201700456, (2017).
41. X.-X. He, J. Zheng, G.-F. Yu, M.-H. You, M. Yu, X. Ning, Y.-Z. Long, Near-field electrospinning: Progress and applications. *J. Phys. Chem. C* **121**, 8663–8678 (2017).
42. A. Lee, H. Jin, H. W. Dang, K. H. Choi, K. H. Ahn, Optimization of experimental parameters to determine the jetting regimes in electrohydrodynamic printing. *Langmuir* **29**, 13630–13639 (2013).
43. H. Liu, S. Vijayavenkataraman, D. Wang, L. Jing, J. Sun, K. He, Influence of electrohydrodynamic jetting parameters on the morphology of PCL scaffolds. *Int. J. Bioprint* **3**, 72–82 (2017).
44. A. Haider, S. Haider, I.-K. Kang, A comprehensive review summarizing the effect of electrospinning parameters and potential applications of nanofibers in biomedical and biotechnology. *Arab. J. Chem.* **11**, 1165–1188 (2018).
45. I. Assaid, D. Bosc, I. Hardy, Improvements of the poly(vinyl cinnamate) photoresponse in order to induce high refractive index variations. *J. Phys. Chem. B.* **108**, 2801–2806 (2004).
46. S. Heidari-Keshel, M. Ahmadian, E. Biazar, A. Gazmeh, M. Rabiei, M. Adibi, A. Soufi M, M. Shabani, Surface modification of *Poly Hydroxybutyrate* (PHB) nanofibrous mat by collagen protein and its cellular study. *Mater. Technol.* **31**, 799–805 (2016).
47. C. W. Lee, M. Horiike, K. Masutani, Y. Kimura, Characteristic cell adhesion behaviors on various derivatives of poly(3-hydroxybutyrate) (PHB) and a block copolymer of poly(3-[RS]-hydroxybutyrate) and poly(oxyethylene). *Polym. Degrad. Stab.* **111**, 194–202 (2015).
48. B. Zhang, B. Seong, V. Nguyen, D. Byun, 3D printing of high-resolution PLA-based structures by hybrid electrohydrodynamic and fused deposition modeling techniques. *J. Micromech. Microeng.* **26**, 025015 (2016).
49. M. Rein, V. D. Favrod, C. Hou, T. Khudiyev, A. Stolyarov, J. Cox, C.-C. Chung, C. Chhav, M. Ellis, J. Joannopoulos, Y. Fink, Diode fibres for fabric-based optical communications. *Nature* **560**, 214–218 (2018).
50. J.-K. Song, K. Do, J. H. Koo, D. Son, D.-H. Kim, Nanomaterials-based flexible and stretchable bioelectronics. *MRS Bull.* **44**, 643–656 (2019).
51. S. Hong, J. Lee, K. Do, M. Lee, J. H. Kim, S. Lee, D.-H. Kim, Stretchable electrode based on laterally combed carbon nanotubes for wearable energy harvesting and storage devices. *Adv. Funct. Mater.* **27**, 1704353 (2017).
52. M. C. George, P. V. Braun, Multicompartmental materials by electrohydrodynamic cojetting. *Angew. Chem. Int. Ed.* **48**, 8606–8609 (2009).
53. J. Choi, D. S. Moon, S. G. Ryu, B. Lee, K. J. Lee, Highly functionalized thermoplastic polyurethane from surface click reactions. *J. Appl. Polym. Sci.* **135**, 46519 (2018).
54. J. Yoon, K. J. Lee, J. Lahann, Multifunctional polymer particles with distinct compartments. *J. Mater. Chem.* **21**, 8502–8510 (2011).
55. S. Bhaskar, J. Hitt, S.-W. Chang, J. Lahann, Multicompartmental microcylinders. *Angew. Chem. Int. Ed. Engl.* **48**, 4589–4593 (2009).
56. J. Lahann, Recent progress in nano-biotechnology: Compartmentalized micro- and nanoparticles via electrohydrodynamic co-jetting. *Small* **7**, 1149–1156 (2011).
57. K.-H. Roh, D. C. Martin, J. Lahann, Biphasic Janus particles with nanoscale anisotropy. *Nat. Mater.* **4**, 759–763 (2005).
58. S. Moon, M. Gil, K. J. Lee, Syringeless electrospinning toward versatile fabrication of nanofiber web. *Sci. Rep.* **7**, 41424 (2017).
59. S. Moon, J. Yun, J. Y. Lee, G. Park, S.-S. Kim, K. J. Lee, Mass-production of electrospun carbon nanofiber containing SiO_x for lithium-ion batteries with enhanced capacity. *Macromol. Mater. Eng.* **304**, 1800564 (2018).
60. S. Moon, K. Park, E. Seo, K. J. Lee, Mass production of functional amine–conjugated PAN nanofiber mat via syringeless electrospinning and CVD. *Macromol. Mater. Eng.* **303**, 1700565 (2018).

Acknowledgments

Funding: This research was supported by National Research Foundation (NRF) grants (NRF-2017R1A4A1015360, 2019R1F1A1058452, and 2013M3A6A5073175). We acknowledge funding under U01CA210152 from the National Cancer Institute and support provided through award EEC-1647837 as part of the Engineering Research Centers Program of the National Science Foundation (CELL-MET). **Author contributions:** S.M, K.J.L. and J.L. conceived the study and co-wrote the manuscript. K.J.L and J.L. supervised the project. S.M. and J.L. panned and performed the experiments, and collected and analyzed the data. L.L. performed the electrical analysis. M.S.J. fabricated PHB scaffold. E.S. synthesized ATPU and performed UV-sensor application. J.H.J. assisted with the analysis of jetting phenomena. **Competing interests:** The authors declare that they have no competing interests. **Data and materials availability:** All data needed to evaluate the conclusions in the paper are present in the paper and/or the Supplementary Materials. Additional data related to this paper may be requested from the authors.

Submitted 2 November 2020
Accepted 25 February 2021
Published 14 April 2021
10.1126/sciadv.abf5289

Citation: S. Moon, M. S. Jones, E. Seo, J. Lee, L. Lahann, J. H. Jordahl, K. J. Lee, J. Lahann, 3D jet writing of mechanically actuated tandem scaffolds. *Sci. Adv.* **7**, eabf5289 (2021).

Science Advances

3D jet writing of mechanically actuated tandem scaffolds

Seongjun Moon, Michael S. Jones, Eunbyeol Seo, Jaeyu Lee, Lucas Lahann, Jacob H. Jordahl, Kyung Jin Lee and Joerg Lahann

Sci Adv **7** (16), eabf5289.
DOI: 10.1126/sciadv.abf5289

Science Advances (ISSN 2375-2548) is published by the American Association for the Advancement of Science, 1200 New York Avenue NW, Washington, DC 20005. The title *Science Advances* is a registered trademark of AAAS.